CORA Cork Open Research Archive
Cartlann Taighde Oscailte Chorcaí

Title	Investigating subphotospheric dissipation in Gamma-Ray Bursts using joint Fermi-Swift observations
Authors	Ahlgren, Björn;Larsson, Josefin;Valan, Vlasta;Mortlock, Daniel;Ryde, Felix;Pe'er, Asaf
Publication date	2019-07-26
Original Citation	Ahlgren, B., Larsson, J., Valan, V., Mortlock, D., Ryde, F. and Pe'er, A. (2019) 'Investigating Subphotospheric Dissipation in Gamma-Ray Bursts Using Joint Fermi–Swift Observations', The Astrophysical Journal, 880(2), 76. (15pp.) DOI: 10.3847/1538-4357/ab271b
Type of publication	Article (peer-reviewed)
Link to publisher's version	https://iopscience.iop.org/article/10.3847/1538-4357/ab271b - 10.3847/1538-4357/ab271b
Rights	© 2019. The American Astronomical Society. All rights reserved. - https://creativecommons.org/licenses/
Download date	2026-10-29 10:11:22
Item downloaded from	https://hdl.handle.net/10468/8780

UCC
University College Cork, Ireland
Coláiste na hOllscoile Corcaigh

The Astrophysical Journal, 880:76 (15pp), 2019 August 1 https://doi.org/10.3847/1538-4357/ab271b
© 2019. The American Astronomical Society. All rights reserved.

Investigating Subphotospheric Dissipation in Gamma-Ray Bursts Using Joint *Fermi*–*Swift* Observations

Björn Ahlgren[1], Josefin Larsson[1], Vlasta Valan[1], Daniel Mortlock[2,3,4], Felix Ryde[1], and Asaf Pe'er[5]
[1] KTH Royal Institute of Technology, Department of Physics, and the Oscar Klein Centre AlbaNova, SE-106 91 Stockholm, Sweden; bjornah@kth.se
[2] Imperial College London, Department of Mathematics, Statistics Section, London SW7 2AZ, UK
[3] Imperial College London, Astrophysics group, Blackett Laboratory, Prince Consort Road, London SW7 2AZ, UK
[4] Stockholm University, Department of Astronomy, and the Oscar Klein Centre AlbaNova, SE-106 91 Stockholm, Sweden
[5] University College Cork, Physics Department, Cork, Ireland
Received 2019 March 22; revised 2019 May 24; accepted 2019 May 29; published 2019 July 26

Abstract

The jet photosphere has been proposed as the origin for the gamma-ray burst (GRB) prompt emission. In many such models, characteristic features in the spectra appear below the energy range of the *Fermi* Gamma-ray Burst Monitor (GBM) detectors, so joint fits with X-ray data are important in order to assess the photospheric scenario. Here we consider a particular photospheric model which assumes localized subphotospheric dissipation by internal shocks in a non-magnetized outflow. We investigate it using Bayesian inference and a sample of eight GRBs with known redshifts which are observed simultaneously with *Fermi* GBM and the *Swift* X-ray Telescope (XRT). This provides us with an energy range of 0.3 keV–40 MeV and much tighter parameter constraints. We analyze 32 spectra and find that 16 are well described by the model. We also find that the estimates of the bulk Lorentz factor, Γ, and the fireball luminosity, $L_{0,52}$, decrease while the fraction of dissipated energy, $\varepsilon_{\rm d}$, increases in the joint fits compared to GBM-only fits. These changes are caused by a small excess of counts in the XRT data, relative to the model predictions from fits to GBM-only data. The fact that our limited implementation of the physical scenario yields 50% accepted spectra is promising, and we discuss possible model revisions in the light of the new data. Specifically, we argue that the inclusion of significant magnetization, as well as removing the assumption of internal shocks, will provide better fits at low energies.

Key words: gamma-ray burst: general – methods: data analysis – radiation mechanisms: thermal

Supporting material: figure sets, machine-readable table

1. Introduction

The prompt phase of gamma-ray bursts (GRBs) is characterized by strongly variable gamma-ray emission that typically lasts less than a minute. While almost all models agree that this emission originates from internal processes in a relativistic jet, the mechanism producing the emission is not understood. GRB spectra are often described using empirical models, particularly a smoothly broken power law known as the Band function (Band et al. 1993). This function has often been interpreted in terms of synchrotron radiation; see e.g., Tavani (1996), Briggs et al. (1999), Abdo et al. (2009), and Zhang et al. (2016). However, it was argued by Preece et al. (1998) that fits with the Band function show that a large fraction of observed spectra are harder than can be accounted for by synchrotron radiation. This has been one of the reasons for considering other emission mechanisms. There are also some GRBs observed with very hard spectra, which can be well described by blackbody or multi-color blackbody models (Ryde 2004; Ryde et al. 2011; Ghirlanda et al. 2013; Larsson et al. 2015). Although pure blackbody emission is clearly too hard to describe most observed spectra, there are several possible broadening mechanisms which soften the low-energy slope of photospheric emission, including geometric effects (Pe'er 2008; Lundman et al. 2013), and subphotospheric dissipation (Rees & Mészáros 2005; Giannios 2006; Pe'er et al. 2006; Beloborodov 2010; Vurm et al. 2011; Chhotray & Lazzati 2015). Photospheric emission also provides a viable explanation for the Yonetoku relation (Yonetoku et al. 2004, 2010), as shown by Ito et al. (2019). See also Parsotan et al. (2018) for further discussion on photospheric emission as an origin of the Yonetoku relation, as well as for the related Amati (Amati et al. 2002) and Golenetskii (Golenetskii et al. 1983) relations.

To evaluate different physical models for the prompt emission it is important to directly fit the models to data. Indeed, considerable work in recent years has shown that inferences about emission processes based on fits with the Band function, including the aforementioned hardness problem, can be misleading (Burgess et al. 2014, 2018; Burgess 2017; Ahlgren et al. 2019; A19 from now on). Examples of previous physical models fitted to data include a physical synchrotron model (fit to GRBs observed by the BATSE instrument; Lloyd & Petrosian 2002), the ICMART model (fit to GRB 080916C; Zhang & Yan 2011), and the external shock model (fit to GRB 141028A; Burgess et al. 2016). Unfortunately, fitting these models to data is generally time consuming, making broad usage difficult. However, there have recently been new developments, with Burgess et al. (2018) showing successful fits to a sample of 19 GRBs using a physical synchrotron model.

Another recent example is provided in A19, where we tested a specific photospheric model for localized subphotospheric dissipation by internal shocks with no magnetic fields (DREAM, introduced in Ahlgren et al. 2015; A15 from now on). We analyzed time-resolved spectra of 36 GRBs observed by the Gamma-ray Burst Monitor (GBM; Meegan et al. 2009) on board the *Fermi Gamma-Ray Space Telescope* and found that ∼30% of the spectra could be well described by the model, with 10 GRBs having at least half of their spectra accepted. The model consistently failed to describe the GRBs with the highest

luminosities, which may be a result of the specific dissipation scenario considered. The level of dissipation was found to be around ∼5%, consistent with the internal shock scenario, and the luminosity and Lorentz factor of the model were found to be correlated. The latter has independently been reported in other studies (Lü et al. 2012; Ghirlanda et al. 2018). In our study there was no correlation between the fitted Band function α and β parameters and any properties of the fits using the DREAM model. The current implementation of the physical scenario is still being improved upon, and the large number of well-described spectra motivates further exploration of the model scenario.

While *Fermi* observes GRB prompt emission over a wider energy range than any other GRB mission, it is limited by its lower-energy bound of 8 keV. Physical models (including DREAM) often predict distinct spectral features below this energy and observations of the prompt emission down to soft X-rays therefore have the potential to be very constraining. For instance, in the case of DREAM, the curvature at low energies is a result of incomplete Comptonization of the seed photon blackbody, which may be located at energies as low as ∼1 keV in the observer frame. The X-ray Telescope (XRT; Burrows et al. 2005) on board the *Neil Gehrels Swift Observatory* observes in the 0.3–10 keV energy band, but the observations are limited by the fact that they typically start ∼100 s after a trigger from the Burst Alert Telescope (BAT). For most GRBs the prompt gamma-ray emission has already ended by this time.

Studies of early XRT observations have shown that the emission is due to a combination of late prompt emission and early afterglow emission from the interaction between the jet and circumstellar medium (O'Brien et al. 2006; Burrows et al. 2007). The former is manifested by flares in the light curve, which have properties similar to the prompt gamma-ray emission (Chincarini et al. 2010). Given these considerations, we note that it is possible to study the prompt emission from soft X-rays to gamma-rays in GRBs for which the *Swift*/XRT light curve is dominated by flares and the prompt gamma-ray emission has a sufficiently long duration.

In previous joint analyses of XRT and GBM prompt emission, Oganesyan et al. (2017, 2018) found that many spectra exhibit a second spectral break at around a few keV. They performed fits using a doubly smoothly broken power law, and interpret their results in terms of synchrotron radiation. Additionally, Nappo et al. (2017) performed a time-resolved joint analysis of data from several instruments, including GBM and XRT, of GRB 151027A, where they detect the presence of a thermal component at low energies. These different results are interesting also from the perspective of photospheric models, as these often have a curvature at energies around a few keV.

In this work we present further investigation of the model presented in A19 by performing joint analysis to data from *Fermi*/GBM and *Swift*/XRT using Bayesian inference. The only difference from the model presented in A19 is a small expansion of the parameter space. We analyze a sample of eight GRBs which have overlapping GBM and XRT observations and known redshifts. The goal is to use the large-energy window offered by the joint observations to provide new constraints on the physical scenario and parameter space of our model. We also want to assess the impact of the XRT data in prompt emission analysis.

In Section 2 we describe the physical scenario and how it is implemented as a numerical model. We describe the data sample and analysis in Sections 3 and 4, followed by a presentation of the results in Section 5 and discussion in Section 6. In Section 7 we summarize our findings. Throughout the paper we assume standard Λ-CDM cosmology using the constants $H_0 = 67.3$, $\Omega_\lambda = 0.685$, and $\Omega_M = 0.315$ (Planck Collaboration et al. 2014).

2. Model

We study a photospheric emission model, in which localized subphotospheric dissipation occurs due to internal shocks. Moreover, we assume no magnetization and ignore off-axis emission and other geometrical effects. The model used in this work is identical to that of A19, apart from a small expansion of the parameter space. For completeness, we here briefly describe the physical scenario and its numerical implementation. For a more detailed description of the model, including validation tests, see A19 and the references given below.

2.1. Physical Scenario

The physical scenario we consider is a hot fireball (for an overview see, e.g., Pe'er 2015), with localized subphotospheric dissipation at a moderate optical depth. We assume that a central engine emits a hot plasma of baryons, electrons, and photons, at a luminosity $L_0 = L_{0,52}10^{52}$ erg s^{-1}. The outflow accelerates due to the thermal pressure from the photons until it obtains its coasting bulk Lorentz factor, Γ. We assume a dissipation radius, $r_d = r_{ph}/\tau = L\sigma_T/(4\pi\tau\Gamma^3c^3m_p)$, where $r_{ph}$is the photospheric radius and τ is the optical depth (see, e.g., Pe'er et al. 2006). The internal shock assumption furthermore implies that $r_d = \Gamma^2 r_0$, where r_0 is the nozzle radius. This relation couples the photon temperature at the dissipation site to Γ, $L_{0,52}$ and τ. At r_d, a fraction $\varepsilon_d\varepsilon_e$ of the bulk kinetic energy of the outflow begins to dissipate to the electrons, and a fraction $\varepsilon_d\varepsilon_b$ to the magnetic fields. The dissipation is assumed to continue until $2r_d$. In the particular scenario considered here, we assume that $\varepsilon_b = 10^{-6}$ and $\varepsilon_e = 0.9$, i.e., that magnetic fields are negligible and that almost all the energy is dissipated to the electrons.We also assume that the heated electrons are Maxwellian distributed. The remaining ∼0.1 ε_d energy is considered not dissipated. The parameterization with ε_d, ε_e, and ε_b is for practical reasons only and the total efficiency in this case is given by $\varepsilon_d\varepsilon_e$. Further, we assume that $\tau = 35$, which means that we test a scenario where the dissipation occurs moderately deep below the photosphere. Tests have shown that this is often a good approximation since many bursts are largely insensitive to this parameter (see A19 for further discussion).

Since we assume a scenario where the dissipation occurs below the photosphere, the heated electrons will interact with the photon field in a non-equilibrium situation. In our model we consider Compton and inverse Compton scattering, pair production, and pair annihilation. In principle we also account for synchrotron and synchrotron self-absorption. However, these effects are very small in the case of negligible magnetization.

For localized dissipation in outflows with negligible magnetization, hadronic collisions (Beloborodov 2010) and internal shocks (Kobayashi et al. 1997; Daigne & Mochkovitch 1998; Rees & Mészáros 2005) have been suggested as possible

dissipation mechanisms. The scenario we consider here is based on the internal shock scenario (Pe'er 2015).

To simulate the physical scenario we use the kinetic code by Pe'er & Waxman (2005), which treats all processes described above. Our treatment does not include any spatial effects, such as geometric broadening (Pe'er 2008; Lundman et al. 2013), or jet hydrodynamics (Lazzati et al. 2009). We also assume that the photosphere is sharp, as opposed to fuzzy (Beloborodov 2011; Bégué et al. 2013). While we restrict ourselves to a specific dissipation scenario, alternative scenarios are also possible; see, e.g., Vurm et al. (2011).

2.2. Table Model

In order to perform fits with the model we construct an XSPEC-compatible table model (Arnaud et al. 1999), which consists of a grid of spectra simulated for different parameter values. Model predictions for parameters between the grid points are obtained by linear interpolation during the fitting. The simulations are costly to perform, which means that we are not able to explore all available parameter space. In A19 we presented a model in three dimensions with 891 grid points, consisting of the level of dissipation, $\varepsilon_{\rm d}$, the luminosity, $L_{0,52}$, and the bulk Lorentz factor, Γ.

For this study we have expanded the model with additional grid points in Γ, extending the range down to 50 from 100 and from 500 up to 1000. We added these grid points to obtain a better coverage of values of Γ inferred from observations (Ghirlanda et al. 2018). We have also added one additional grid point in $L_{0,52}$, at 1000. This grid point has been added to account for the possibility of very luminous bursts with narrow jets. There are no differences in the underlying code used to construct the grid. The model is now spanned by

$$\begin{aligned}\Gamma &= 50, 100, 150, 200, 250, 300, 350,\\ &\quad 400, 450, 500, 600, 700, 800, 900, 1000\\ L_{0,52} &= 0.1, 0.5, 1, 5, 10, 50, 100, 200, 300, 1000\\ \varepsilon_{\rm d} &= 0.01, 0.025, 0.05, 0.75, 0.1, 0.15,\\ &\quad 0.2, 0.25, 0.3, 0.35, 0.4.\end{aligned}$$

As noted in A19, high values of $\varepsilon_{\rm d}$ would yield a re-acceleration of the outflow, which is not accounted for in our code. Thus, we limit $\varepsilon_{\rm d}$ to values where the effects of such a re-acceleration are expected to be small. In A19 we demonstrated that the finite resolution of the grid introduces systematic uncertainties of 5%–8% in the best-fit parameter values, which is smaller than the typical statistical uncertainties. When creating a table model we also obtain one parameter for the redshift and one for the normalization. The latter is set by the redshift as $d_{\rm L}^2(z=1)/d_{\rm L}^2(z_{\rm obs})$, where $d_{\rm L}(z)$ is the luminosity distance. Both of these parameters are kept fixed in the fits.

In line with previous work, we denote this version of the table model DREAM1.3, using the naming convention introduced in A19.[6] Throughout this work, "model" refers to DREAM1.3, unless otherwise stated. The underlying physical model scenario is referred to explicitly as "physical scenario," to avoid confusion. The physical scenario we are testing is subphotospheric dissipation with localized dissipation at a moderate optical depth in a jet with negligible magnetization.

[6] This naming convention was introduced because of the plan to make the model publicly available. It is then convenient to be able to distinguish between different versions of the model used in different articles.

3. Observations

3.1. Sample Selection

We examine all GRBs with a known redshift which have overlapping observations in the *Swift* XRT and *Fermi* GBM detectors, up until 2018 November 1. As mentioned in Section 2.2, the redshift is needed in order to obtain the luminosity distance for the model. We also require the overlapping interval to be at least 5 s long and that it is possible to bin the XRT data into at least two time bins using the method outlined in Section 4 below. Finally, we require that at least one time bin has a signal-to-noise ratio (S/N) in one GBM NaI detector of at least 3, as described in Section 4 (the S/N in the XRT is always higher than this). Note that we do not use data from the BAT, also on board the *Swift* satellite, due to its narrower energy range (15–150 keV) compared to GBM. Contrary to the burst sample in A19 we do not perform a fluence cut in this sample selection. These criteria result in a relatively small sample of eight GRBs, the properties of which are summarized in Table 1. In Figure 1, we show the count rate light curves of all bursts, including both GBM and XRT data.

XRT observations typically start ∼100 s after the GBM trigger (corresponding to the time it takes for *Swift* to slew following a BAT trigger). For most GRBs in the sample the GBM and XRT data overlap for 40–50 s at the end of the prompt emission. However, there are two exceptions: GRB 080928 and GRB 140206A. These bursts have XRT data from the start of the GBM trigger. This is because BAT triggered on precursors at −204 s and −56 s, respectively, relative to the GBM trigger (not included in Figure 1). Figure 1 also shows that all the XRT light curves contain flares, as expected if the emission belongs to the prompt phase. In most cases the GBM and XRT light curves are clearly correlated. However, we note that this correlation is less prominent in GRB 100814A and GRB 100906A. This could be due to that the GBM data are particularly weak in these intervals. Additionally, in GRB 151027A, there is a clear delay in the XRT with respect to the GBM.

Comparing with the sample in A19, six bursts (GRB 100728A, GRB 100814A, GRB 100906A, GRB 140206A, GRB 140512A, and GRB 151027A) are contained in both samples. In A19 we found that only two of these bursts, GRB 140512A and GRB 151027A, had more than half of their analyzed time bins well described by our model. We discuss this further in Section 6.3.

3.2. Data Reduction

3.2.1. Fermi Data

In the *Fermi* analysis we use data observed with the GBM. Specifically we use the time-tagged event data from both the NaI and BGO detectors. We include up to three NaI detectors with an angle of incidence less than 60° in the analysis, as well as the BGO detector with the lowest angle of incidence (Bhat et al. 2016). However, there is one exception where we have excluded an additional NaI from the analysis. In GRB 151027A we use only the NaI0 (19°) and NaI3 (37°) detectors, ignoring the n6 (25°) detector, which has a significantly different spectrum in several bins (example in Figure 2). This may be due to blockage of the detector by a part of the satellite, or some other issue with the detector response (Goldstein et al. 2012).

Table 1
Summary of Data Sample, Including Which GBM Detectors Were Used for the Different Bursts and for How Long We Have Overlapping Data of GBM and XRT

GRB	Redshift	GBM Detectors	$T_{90,\mathrm{GBM}}$ (s)	$T_{0,\mathrm{XRT}}$[a] (s)	Overlap (s)	$N_{\mathrm{H,gal}}$ (10^{22} cm^{-2})	$N_{\mathrm{H,intr}}$ (10^{22} cm^{-2})	PC Data Interval (s)
080928	1.692	NaI3, NaI6, NaI7, BGO0	14.3	−27.2	37	0.072	$0.47^{+0.16}_{-0.16}$	4262–12612
100728A	1.567	NaI0, NaI1, NaI2, BGO0	165.4	134.2	44	0.165	$3.16^{+0.44}_{-0.42}$	1333–7548
100814A	1.44	NaI7, NaI8, BGO1	150.5	96.1	55	0.018	$0.00^{+0.09}$	5923–34841
100906A	1.727	NaI8, NaI11, BGO1	110.6	83.8	27	0.353	$1.24^{+0.63}_{-0.64}$	10592–99797
140206A	2.73	NaI10, NaI11, BGO1	27.3	−5.6	34	0.070	$1.08^{+0.51}_{-0.44}$	126574–956006
140512A	0.725	NaI0, NaI1, NaI3, BGO0	148.0	108.9	41	0.147	$0.31^{+0.06}_{-0.05}$	4581–12859
151027A	0.81	NaI0, NaI3, BGO0	123.4	93.4	18	0.037	$0.58^{+0.13}_{-0.13}$	11633–63739
161117A	1.549	NaI1, NaI2, NaI10, BGO0	122.2	72.5	53	0.043	$0.99^{+0.38}_{-0.34}$	46352–69247

Note. The overlap indicates the overlap between the start of the XRT data and the *Fermi* T_{90}. Redshifts were acquired from http://www.mpe.mpg.de/~jcg/grbgen.html. We also present the values of the column densities, $N_{\mathrm{H,gal}}$ and $N_{\mathrm{H,intr}}$. The PC data interval indicates the time interval after the BAT trigger used when determining $N_{\mathrm{H,intr}}$.
[a] With respect to the GBM trigger.

The background is determined from a polynomial fit to the light curve, which gives a model for the background with Gaussian errors. We account for temporal evolution of the background spectrum and the changing position of the spacecraft by using rsp2 response files when available.

3.2.2. XRT Data

For the spectral analysis of XRT data we use observations taken in the windowed timing (WT) mode, which is used when the count rate is high. We also download late-time photon counting (PC) data for each GRB, in order to determine the intrinsic column density ($N_{\mathrm{H,intr}}$) for the absorption at low energies (see Section 4.3).

The WT data are downloaded as locally reprocessed data from the UK *Swift* Science Data Centre XRT GRB repository.[7] We create time bins of the spectrum locally, as described in Section 4. These time bins are then used to specify the limits on time-sliced spectra, which we create and download from the online repository. All spectra are grouped such that each energy bin contains at least one count. This is the recommended approach when fitting with the cstat fit statistic in XSPEC.[8] The background is supplied online when downloading the data. The background spectrum is constructed by sampling in an area around the burst position and it is assumed to be Poisson distributed.

All XRT spectra were checked for known calibration issues following Valan et al. (2018). This includes redistribution issues, which may cause a bump below 1 keV and/or a turn-up below ∼0.6 keV. Pile-up is automatically dealt with by the online tool. We find redistribution issues in GRB 100728A and GRB 151027A. We accommodate these by ignoring channels below 0.6 keV in these bursts.

4. Data Analysis

We perform a time-resolved spectral analysis using time bins defined by a Bayesian blocks binning (Scargle et al. 2013) of the XRT data. We use battblocks[9] with default settings to bin the XRT light curve. The GBM data are binned in matching time bins. We use HEASARC's online tool xTime[10] to convert between *Swift* mission time and *Fermi* mission time.

We calculate the S/N of each spectrum as described in Vianello (2018). For the GBM data we use Poisson–Gaussian significance, whereas for the XRT data we use Poisson–Poisson significance. The XRT data consistently have a high S/N, but as in A19 we choose to apply an S/N cut to the GBM data in order to only analyze spectra that contain a significant signal in GBM. Thus, we only analyze spectra with S/N > 3 in the brightest NaI detector. This leaves us with 32 out of 51 time-resolved spectra to analyze.

4.1. Fitting

We set up the analysis as a Bayesian inference procedure. Bayes' theorem states that the posterior probability is

$$\Pr(\theta|y) = \frac{\Pr(\theta)\Pr(y|\theta)}{\int \Pr(\theta)\Pr(y|\theta)d\theta} \propto \Pr(\theta)\Pr(y|\theta),$$

where θ are our model parameters and y the observed data. $\Pr(\theta)$ is the prior, $\Pr(y|\theta)$ the likelihood, and the denominator the marginalized likelihood (also referred to as the evidence). We use PyMultiNest (Buchner et al. 2014), a python implementation of MultiNest (Feroz & Hobson 2008; Feroz et al. 2009, 2013), to sample from the model posterior using 600 live points. We have chosen this particular number by testing the analysis with different numbers of live points to ensure stability.

For the *Fermi* data, we consider the energy ranges 8–1000 keV and 200 keV–40 MeV for the NaI and BGO detectors, respectively. We also ignore the interval 30–40 keV in the NaI detectors, because of the iodine *K*-edge (Bissaldi et al. 2009). For the XRT data we consider the nominal energy range 0.3–10 keV. However, we lower the high-energy limit in cases when the signal stops below 10 keV. Additionally, the low-energy limit is modified in the presence of calibration issues, as described in Section 3.2.2 (which affects GRB 100728A and GRB 151027A).

[7] http://www.swift.ac.uk/xrt_live_cat/
[8] See the XSPEC manual appendix https://heasarc.gsfc.nasa.gov/xanadu/xspec/manual/XSappendixStatistics.html.
[9] Heasoft version 6.17.
[10] https://heasarc.gsfc.nasa.gov/cgi-bin/Tools/xTime/xTime.pl

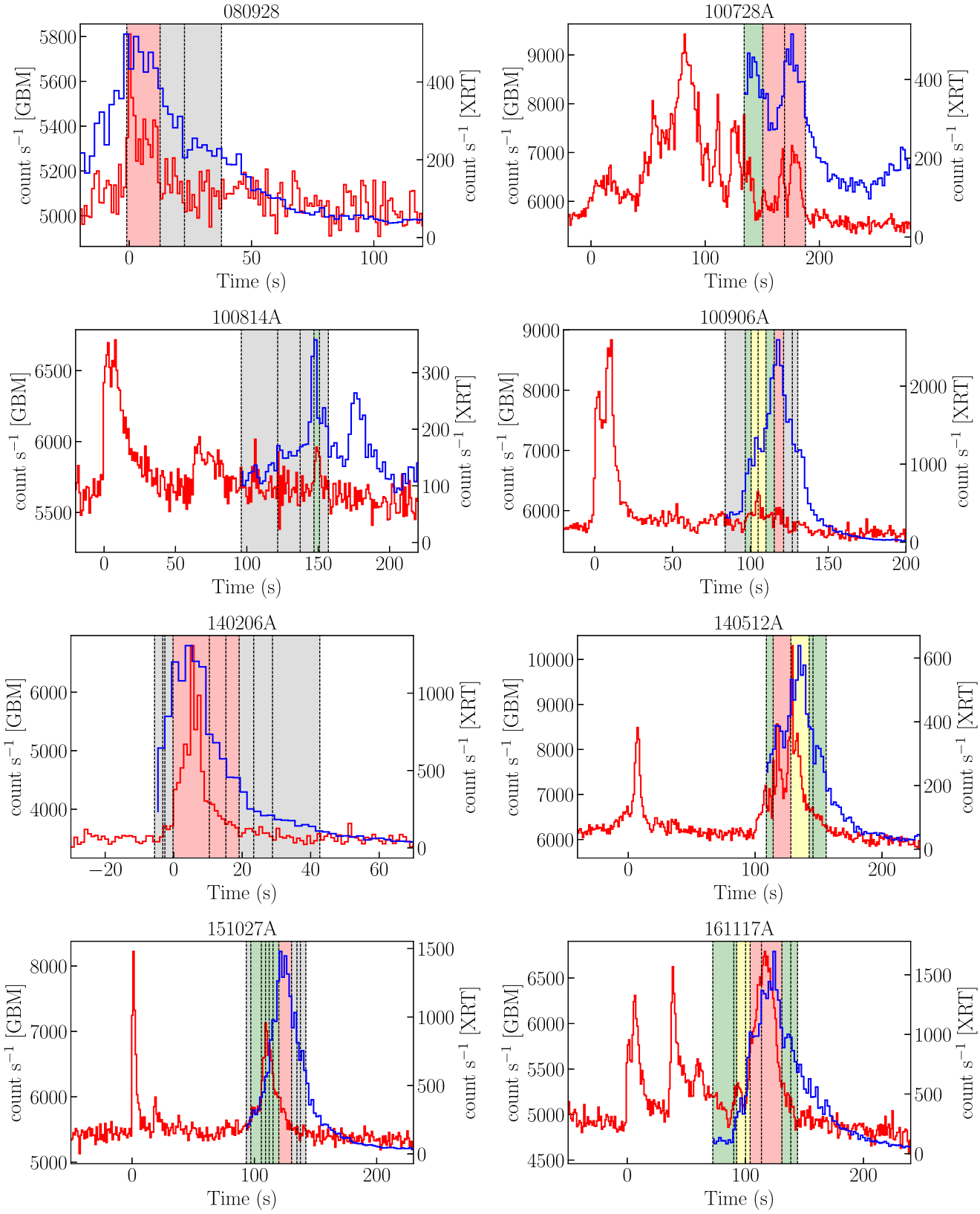

Figure 1. Count rate light curves for all GRBs in our sample. GBM and XRT data are marked in red and blue, respectively. The time refers to the GBM trigger. The count rate for the GBM is the summed count rate for all NaI and BGO detectors used in the analysis. The GBM and XRT light curves are binned in 1 s and 2 s bins, respectively. The start and end times for all time bins identified by the Bayesian blocks algorithm in the overlapping region are marked by dashed black lines. Gray shading indicates that the bin has not been analyzed due to low S/N in the GBM (see Section 4). Green shading indicates that the fit passed the posterior predictive check (PPC; see Section 4.4). Similarly, red shading indicates that the fit did not pass the PPC. Yellow shading indicates that the fit passed the PPC but is considered rejected on other grounds (see Sections 5.2 and 6.1). Note that the XRT light curves are background subtracted, whereas the GBM light curves include background.

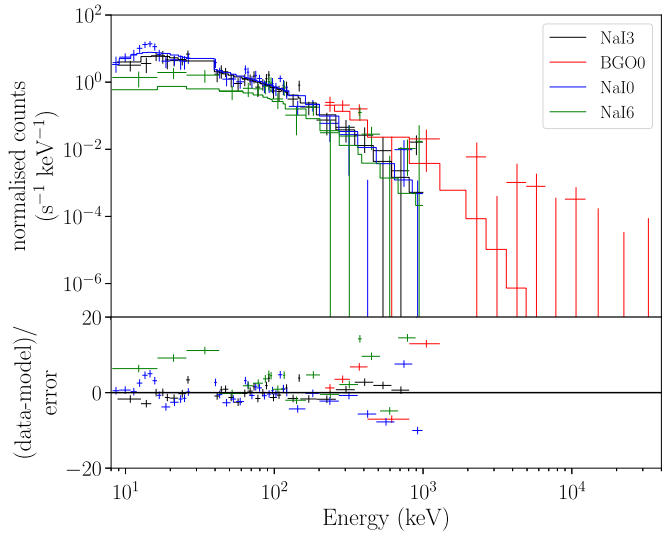

Figure 2. Counts spectrum of GRB 151027A in the time interval 115.2–120.0 s, fitted with a cutoff power-law model. The detectors corresponding to the different data sets are given by the legend. There are large and systematic discrepancies between the best-fit model and the data in the NaI6 detector. This is caused by some unknown issue with the detector response. This detector is therefore excluded from the analysis.

For the *Fermi* data we use a likelihood for a Poisson-distributed signal with Gaussian background. In XSPEC the corresponding statistic is known as pgstat (for a description of pgstat see, e.g., Burgess et al. 2018). For the XRT data we adopt the Cash statistic (Cash 1979), for data with a Poisson signal and background. In XSPEC this statistic is referred to as cstat. Note that pgstat and cstat denote the log likelihood, $\log[\Pr(y|\theta)]$, for the respective data sets. For the joint analysis we consider the fit statistic as the sum of the pgstat and cstat statistics. We perform the analysis using PyXspec, a python implementation of HEASARC's XSPEC 12.8.1g (Arnaud 1996).

The GBM detectors are calibrated with a relative uncertainty on the order of 10% in effective area (Bissaldi et al. 2009). In A19 we found that the best-fit parameter values did not change significantly whether or not we allowed for an effective area correction between the GBM detectors. There is no information on the possible difference in effective area calibration between GBM and XRT. However, we expect that the uncertainty is greater between GBM and XRT than between the GBM detectors. We thus keep the relative normalization between the GBM detectors fixed to unity, whereas we introduce a free relative normalization parameter, $N_{\rm R} = {\rm norm}_{\rm XRT}\,{\rm norm}_{\rm GBM}^{-1}$, between the GBM and XRT data (also referred to as the cross-calibration constant). We let this parameter be fit separately in each time bin.

4.2. Priors

We choose most of our priors to be uninformative. For the luminosity, $L_{0,52}$, and the level of dissipation, $\varepsilon_{\rm d}$, we choose log-uniform priors. This means that each decade in these parameters corresponds to an equal prior probability. For the Lorentz factor, Γ, we choose a uniform prior.

Finally, for the effective area correction between the two instruments, $N_{\rm R}$, we choose a normal distribution prior centered around 1 with a standard deviation of 0.1. Thus, we have

$$\Pr(\log\varepsilon_{\rm d}) = U(0.01,\,0.4)$$
$$\Pr(\log L_{0,52}) = U(0.1,\,1000)$$
$$\Pr(\Gamma) = U(50,\,1000)$$
$$\Pr(N_{\rm R}) = \mathcal{N}(\mu = 1,\,\sigma = 0.1).$$

4.3. Absorption

When analyzing X-ray data below 2 keV, Galactic as well as intrinsic (extragalactic) absorption becomes relevant. We account for this absorption by using the multiplicative XSPEC models *tbvarabs* (for Galactic absorption) and *ztbabs* (for intrinsic absorption). We use the values of the solar abundance vector from Wilms et al. (2000) and the cross-section values listed in Verner et al. (1996). We obtain the weighted total Galactic column density, including the molecular component, $N_{\rm H,gal}$, from the *Swift* $N_{\rm H,tot}$ online tool[11] (Willingale et al. 2013). In the case when the fraction of molecular hydrogen lies in the range of 10%–30% we have replaced the *tbvarabs* model by *tbabs*, where the fraction of molecular hydrogen is fixed to 20%. This is the case for GRB 080928, GRB 151027A, and GRB 161117A.

We determine the intrinsic absorption by fitting late-time PC data with a tbabs∗ztbabs∗pow model. At late times the XRT data are dominated by afterglow emission. These data are fainter and are thus captured in PC mode. Pure afterglow spectra are typically well described by power laws, and at late times we expect little spectral evolution (e.g., Racusin et al. 2009). Thus, this is a good method to determine the intrinsic absorption in a way that does not introduce any degeneracy between the spectral model we wish to test and the absorption. For each burst we create a time-averaged spectrum consisting of as late PC data as possible. In order to avoid spectral evolution we also require the light curve at these times to be well described by a power law without any breaks. We use the light-curve fits from the online catalog[12] to choose these time intervals, which we present in Table 1. The fitting to determine $N_{\rm H,intr}$ is performed using XSPEC's native maximum-likelihood scheme.

Both $N_{\rm H,gal}$ and $N_{\rm H,intr}$ are assumed constant for the duration of the burst and kept fixed in all fits with the DREAM model. In Table 1 we summarize the values of $N_{\rm H,gal}$ and $N_{\rm H,intr}$ used. Comparing to the $N_{\rm H,intr}$ distributions of Campana et al. (2012), we note that the value for GRB 100728A is at the high end of the distribution. Additionally, for GRB 100814A, we find values of $N_{\rm H,intr}$ consistent with 0.

4.4. Posterior Predictive Checks

Since we are performing a Bayesian analysis we can use posterior predictive checks (PPCs; Meng 1994; Gelman et al. 1996; Lynch & Western 2004; Gelman & Shalizi 2013) to assess the quality of our fits. We draw replicated data from the posterior predictive distribution (PPD) using the XSPEC command "fakeit." We then use this new data to assess the quality of our spectral fits. The PPD is the probability of observing some replicated data, conditioned on the observed

[11] http://www.swift.ac.uk/analysis/nhtot/index.php
[12] http://www.swift.ac.uk/xrt_live_cat/

data, and can be written as

$$p(y^{\rm rep}|y) = \int p(y^{\rm rep}|\theta)p(\theta|y)d\theta,$$

where θ, y, and $y^{\rm rep}$ are the model parameters, observed data, and replicated data, respectively. $p(\theta|y)$ is the posterior from which we sample using MultiNest. Thus it is easy to construct a posterior predictive p-value (*ppp*-value),

$$p_{\rm b} = \Pr(T(y^{\rm rep}) > T(y)|y),$$

which corresponds to the classical p-value averaged over the posterior, $p(\theta|y)$, and where T is a test statistic (Rubin 1984). We let T be the fit statistic and calculate $p_{\rm b}$ for each fit based on 1000 realizations from the PPD. We consider a fit rejected if $p_{\rm b} < 0.05$.

We stress that an accepted fit only indicates that we cannot reject the fit at the given significance level. It does not mean that the model necessarily can fully describe the data. Additionally, the *ppp*-value of a rejected fit does not tell us how or where the model fails to describe the data. There are many variants of PPCs which can be used to assess the model fitness. We complement our current choice of PPC with manual inspection of posteriors and fits.

5. Results

In this section we present the results of the Bayesian analysis described in Section 4. When performing Bayesian inference we prefer to consider the posterior in its entirety. However, it is often convenient to also use point estimates, here particularly when comparing to the results of A19 and to give an overview of the results in a table. Thus, for point estimates we use the mean of the marginalized posterior for the parameter in question. The associated uncertainties correspond to the 1σ credible interval centered around the mean symmetrical in terms of cumulative likelihood. In Figure 3 we present examples of corner plots from an accepted and rejected fit, respectively. In Figure 4 we show the corresponding fits in data space. Corner plots showing the full posterior of all fits are available as online material. Additionally, online we also provide plots corresponding to those in Figure 4 for all accepted fits.

5.1. Accepted Fits and Parameter Estimates

A total of 32 time bins were analyzed (17 spectra were not analyzed due to $S/N < 3$ in the GBM), with 21 bins being accepted under the PPCs presented in Section 4.4. In Table 2 we summarize the number of accepted bins for each burst in our sample. We also provide an additional column of spectra which are accepted after further examination of the posterior and fits. This leaves a total of 16 accepted spectra, as presented further in Section 5.2. In Table 3, we present the point estimates of all fits accepted under the PPC. We note that GRB 140512A, GRB 151027A, and GRB 161117A have at least half of the analyzed time bins accepted while having more than one analyzed spectrum (see Figure 1).

In Figure 5 we show the distribution of the relative normalization parameter, $N_{\rm R}$. We note that these values are generally larger than unity, as discussed further in Section 5.2 below. There are too few analyzed and accepted bins to make any reliable inferences about the temporal evolution. However, as can be seen in Table 3, the parameter estimates do not vary erratically throughout a burst. Additionally, we note that the parameters evolve according to the trends we observed in A19. There the most prominent trends were found to show that $L_{0,52}$ follows the light curve.

5.2. The Impact of XRT Data

To examine how the XRT data affect the fits we also perform the analysis with the GBM data only. In Figure 6 we show how parameter estimates change depending on whether we include XRT data in the analysis. It is clear that there are systematic differences in all parameters, although it is most striking for $\varepsilon_{\rm d}$ and Γ. The effect is especially prominent for Γ, with all estimates of Γ decreasing as we introduce XRT data. For $\varepsilon_{\rm d}$ we note that there is a tendency that estimates are higher when we include XRT data. We stress that the parameter estimates with and without XRT data are still consistent within 3σ uncertainties in the majority of cases.

However, five fits remain with non-overlapping posteriors at this level. The spectra in question are GRB 100906A (time bins 3 and 4), GRB 140512A (time bin3), and GRB 161117A (time bins 3 and 4). This indicates that the model cannot describe these data adequately. These fits are not rejected by the PPC since it only considers the overall spectral shape, and not the consistency of different subsets of the data. In Figure 7 we show an example of these non-overlapping posteriors for a spectrum from GRB 100906A. The fact that the posteriors in the left panel are disjunct indicates that the joint fit to GBM–XRT is rejected by the fit in the GBM energy range, and vice versa. We therefore treat these spectra as rejected, even though they passed the PPC. These fits are marked in yellow in Figure 1. We comment on this further in Section 6.1. In Figure 7 we also show an example of posteriors that is more representative of the accepted sample as a whole, where there is significant overlap of the posteriors. Additionally, this figure illustrates that the quality of the constraints improve significantly when XRT data are added. This is a result of both the increased energy range and the quality of the XRT data.

In Table 2, we also present the number of fits which passed the PPC when we did not include the XRT data. Not surprisingly, we note that we obtain additional accepted fits when we remove the XRT data (two extra spectra pass the PPC). This is because the model becomes less constrained, making it harder to reject the fits. However, most fits remain accepted when XRT data are introduced, indicating that the model is overall consistent with the XRT data. It is no surprise that there are spectra which are poorly described by the model. As already found, based on fits to GBM data in A19, GRB 100728A and GRB 140206 are not well described by the model.

In order to illustrate why the parameters change when XRT data are added, we show in Figure 8 the best-fit model to the eighth time bin of GRB 161117A when the analysis has been performed with and without the XRT data (right and left panels, respectively). We let the best fit be represented by the model at the posterior mean. In this example the best-fit model for the GBM data clearly under-predicts the XRT data (left panel). We note that the posteriors have significant overlap within the 3σ credible region (right panel).

Further, we find a similar excess of counts at low energy in the majority of spectra. This is consistent with our finding of the cross-calibration constant generally being larger than unity (see Figure 5). This is because the cross-calibration constant is

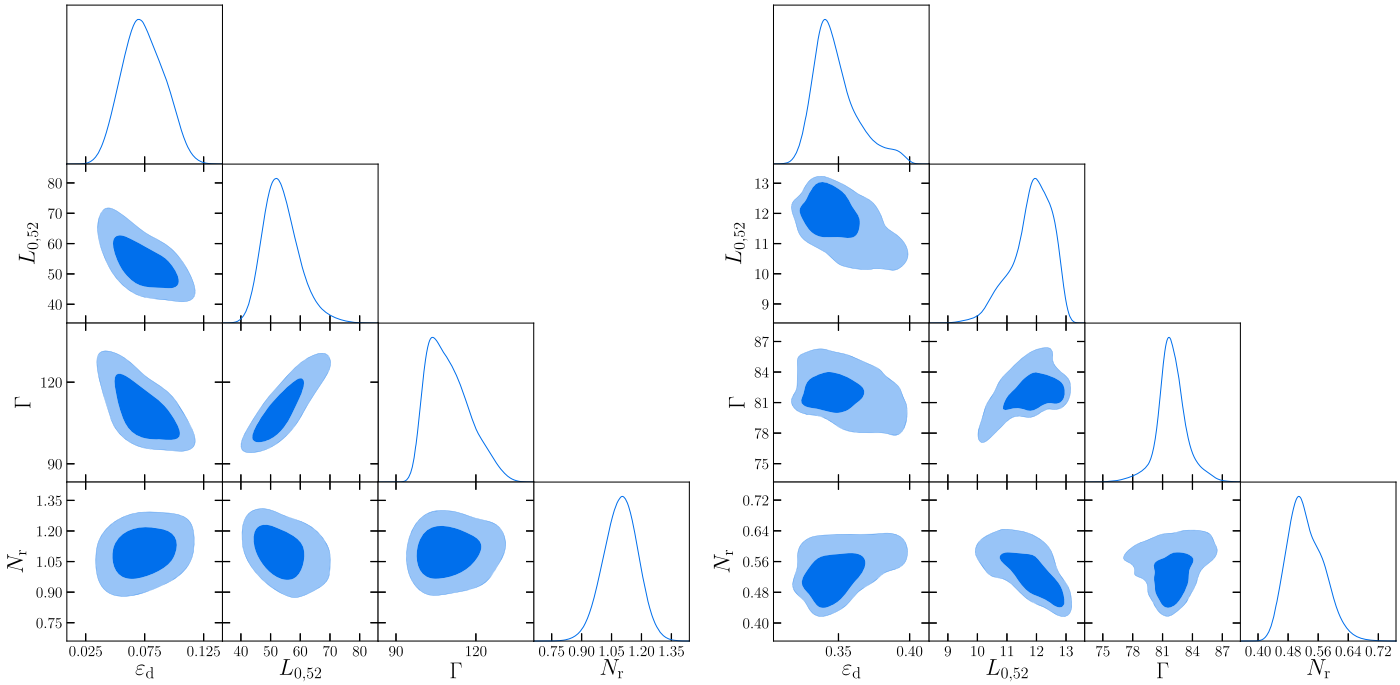

Figure 3. Corner plots showing the full posterior for GRB 100906A at 96.8–100.5 s and GRB 080928 at −1.0–12.6 s, in the left and right panel, respectively. The former passed the PPC, whereas the latter did not. The different contours show the highest posterior density (HPD) regions corresponding to 68% and 95% of the probability volume of the joint posterior distributions. The axes of all corner plots are scaled to show the part of the parameter space where the posterior is non-zero. The plots were generated using the python package getdist. The complete figure set of corner plots for all analyzed spectra (32 images) is available in the online journal.

(The complete figure set (32 images) is available.)

often able to account for some of this excess. For the remaining counts, the logic of the change in parameters is that Γ decreases in order to accommodate the need for additional low-energy counts, which shifts the spectrum to lower energies. In order to maintain the spectral peak, ε_d increases. $L_{0,52}$ decreases to adjust the low-energy slope and to preserve the total energy in the spectrum.

6. Discussion

We have studied a specific version of the subphotospheric dissipation model assuming localized dissipation due to internal shocks ($r_d = \Gamma^2 r_0$) in a flow with negligible magnetization. In A19 we found that this model was unable to describe the brightest part of the GRB population. Since characteristic features in the model occur below the GBM energy range, we have in this paper included data in the soft X-ray range in order to further constrain the model. We find that 50% of the analyzed spectra can be described by the model. Below we discuss these results.

We begin the discussion by considering possible uncertainties in the analysis and the impact these may have on the results (Section 6.1). This also includes a discussion of the limitations of the PPC and additional evaluation of the fits. We then examine what differentiates accepted and rejected fits (Section 6.2). This is followed by a comparison to the results of A19 (Section 6.3). We also discuss the possibility of additional emission components in the XRT data (Section 6.4.1). Finally, we discuss the implications of these results for DREAM, and what changes to the subphotospheric dissipation scenario can be made to accommodate this (Section 6.4.2).

6.1. Uncertainties in the Analysis

The main uncertainties in the analysis are the relative normalization, N_R, and the intrinsic absorption, $N_{H,intr}$. We have investigated the effect of allowing for larger values of N_R by changing its prior to $\mathcal{N}(\mu = 1, \sigma = 0.5)$. Only six of 32 spectra have a marginalized posterior mean for N_R which changes more than 10% when we use this prior. Furthermore, Oganesyan et al. (2017) find that the relative calibration between *Swift* and GBM data agrees within 15%. This is compatible with our original prior, and supports the conclusion that the relative calibration differences have been adequately accounted for. Additionally, tests show that the results are not sensitive to our choice of priors for the other parameters.

We also examined the sensitivity of the results to the value of $N_{H,intr}$. We did this by performing the analysis using the 1σ lower and upper bounds on $N_{H,intr}$ from Table 1. Using the lower bounds of $N_{H,intr}$, only one fit changes any of its parameter estimates (i.e., the mean of the corresponding marginalized posterior) by more than 10%. Similarly, only two fits change when using the upper bounds. These spectra are GRB 080928 at −0.982–12.637 s for high absorption and GRB 100906A at 115.367-121.375 s for both high and low absorption. Both of these spectra are rejected in the original analysis. This indicates that our results are also robust to uncertainties in $N_{H,intr}$.

Using Bayesian inference, information about degeneracies in the model fits is available through the posteriors. Inspecting the corner plots of all fits, we note that there is a tendency to a Γ–ε_d degeneracy. However, it is sufficiently weak to indicate that the changes in Γ and ε_d that we observe in Figure 6 when including XRT data are not caused primarily by model degeneracies.

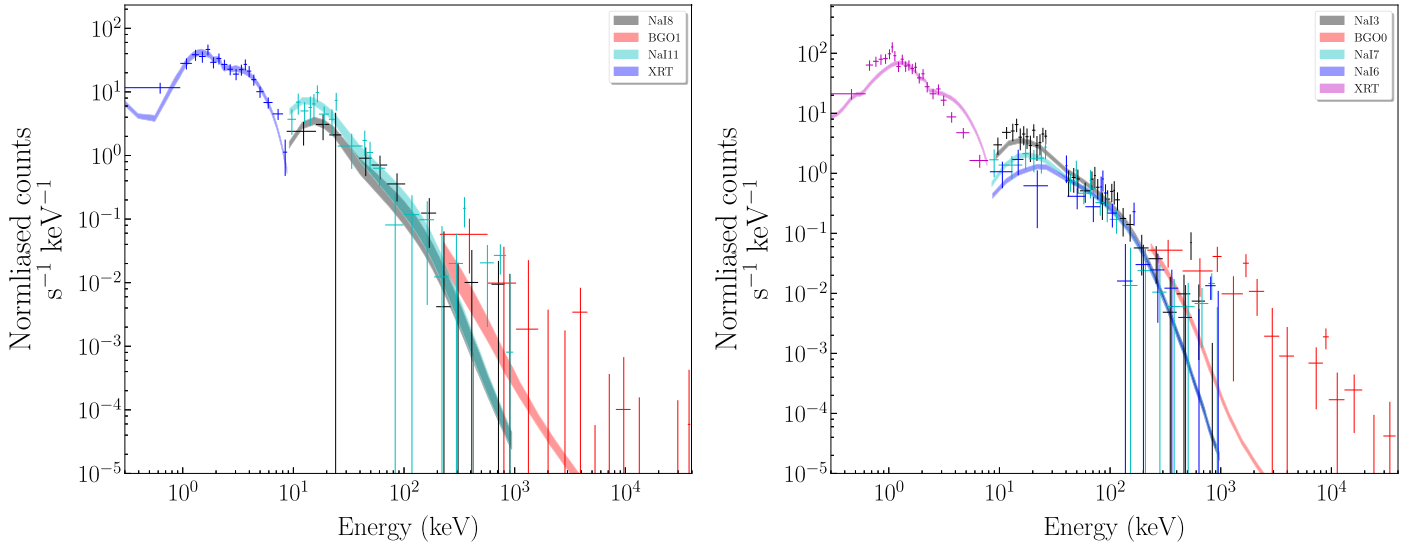

Figure 4. 95% point-wise credible bands of the model shown together with observed counts for GRB 100906A at 96.8–100.5 s and GRB 080928 at −1.0–12.6 s, in the left and right panel, respectively. These are the fits corresponding to the corner plots in Figure 3. Note that the fit in the left panel passed the PPC whereas the fit in the right panel did not. The legend shows which credible band corresponds to which detector. The data have been visually re-binned to 2σ in the GBM data and 5σ in the XRT. The complete figure set for all accepted fits (16 images) is available in the online journal.

(The complete figure set (16 images) is available.)

Table 2
Number of Analyzed Time-resolved Spectra for Each Burst, Together with the Number of Bins That Passed the PPC as Described in Section 4.4

GRB	Analyzed	Accepted (PPC) (GBM+XRT)	Accepted (total) (GBM+XRT)	Accepted (total) (GBM)
080928	1	0	0	1
100728A	3	1	1	1
100814A	1	1	1	1
100906A	5	4	2	4
140206A	3	0	0	0
140512A	5	4	3	5
151027A	6	5	5	5
161117A	8	6	4	6
Σ	32	21	16	23

Note. The fourth column shows the number of accepted spectra after additional consideration has been taken of the posterior distributions and manual inspection of the fits. The fifth column shows the number of bins which are accepted when we consider GBM data only.

However, there is a slightly stronger degeneracy present in Γ–$L_{0,52}$. This is interesting given the Γ–$L_{0,52}$ correlation found in A19. Upon closer inspection we find that this degeneracy is generally small and it was demonstrated in A19 that the correlation is not caused by model degeneracies. There is also a weak degeneracy between $\varepsilon_{\rm d}$ and $L_{0,52}$. This is not surprising given that $\varepsilon_{\rm d}L_{0,52}$ sets the total energy in the spectrum, which is expected to remain constant. Notably, we find no degeneracies between the cross-calibration constant, $N_{\rm R}$, and the other fit parameters.

Regarding the PPC, the chosen *ppp*-value threshold of $p_{\rm b} > 0.05$ will naturally affect the number of accepted spectra. However, we note that the number of spectra do not vary much for small alterations of $p_{\rm b}$, with 21 and 22 accepted spectra for $p_{\rm b} > 0.1$ and $p_{\rm b} > 0.01$, respectively (compared to the 21 accepted spectra at $p_{\rm b} > 0.05$). Thus, despite the small number of analyzed and accepted spectra, our conclusions are not particularly sensitive to the choice of threshold value in the PPC.

As noted in Section 5.2, 5 spectra exhibit significant ($>3\sigma$) inconsistencies between the posteriors from the joint GBM–XRT fits and the GBM-only fits (indicated with yellow shading in Figure 1). Manual inspection shows that these fits deteriorate when XRT data are added, but not enough to cause the PPC to reject the fits. However, the posteriors are sufficiently inconsistent for us to label these fits as rejected for the purpose of this analysis. The fact that the fits still pass the PPC is likely a result of the model's flexibility and the relatively low S/N of the GBM data. This may also be affected by calibration uncertainties.

6.2. Accepted and Rejected Fits

In order to investigate why the model fails to describe about half of the analyzed spectra we search for systematic trends between whether a fit is rejected and the properties of the data. We find only weak correlations between whether a fit is rejected and its corresponding parameter estimates. As shown in Figure 9, there is a tendency of rejecting fits as the model luminosity becomes larger. It also appears that fits with the most extreme values of the cross-calibration constant, $N_{\rm R}$, are rejected (see Figure 10). Although there are not enough data points to ascertain any statistically significant correlations, the luminosity relation is well-known from A19. Furthermore, a cross-calibration constant that deviates significantly from unity suggests that the model cannot adequately describe the data and is compensating for it by improbable values of the artificial normalization parameter. Thus, these correlations are not surprising. There is also an indication that the rejected fits coincide with the peaks of the light curves (see Figure 1). This is likely a result of the model's difficulty in describing spectra with a high luminosity. It could also indicate that the XRT peak flux is dominated by another emission mechanism (discussed further in Section 6.4.1). However, as this trend is not clear for

Table 3
Point Estimates of Model Parameters and r_d for All 21 Fits That Passed the PPC in Our Sample

GRB	Time Bin (s)	ε_d	$L_{0,52}$	Γ	r_d (10^{12} cm)	N_r
100728A	134.2-150.5	$0.38^{+0.01}_{-0.01}$	$15.7^{+0.6}_{-0.6}$	$89.5^{+1.3}_{-1.3}$	$11.0^{+0.4}_{-0.4}$	$1.32^{+0.07}_{-0.07}$
100814A	147.0-150.9	$0.27^{+0.05}_{-0.05}$	$11.9^{+1.4}_{-1.7}$	$96.9^{+1.5}_{-3.8}$	$6.6^{+0.5}_{-0.4}$	$0.98^{+0.09}_{-0.09}$
100906A	96.8-100.5	$0.07^{+0.02}_{-0.02}$	$53.6^{+5.8}_{-5.8}$	110^{+8}_{-8}	$20.6^{+2.9}_{-2.9}$	$1.10^{+0.08}_{-0.09}$
100906A	100.5-105.0	$0.09^{+0.02}_{-0.02}$	$72.5^{+7.0}_{-7.2}$	114^{+8}_{-9}	$25.2^{+4.0}_{-3.8}$	$1.00^{+0.08}_{-0.08}$
100906A	105.0-110.0	$0.08^{+0.02}_{-0.02}$	$74.8^{+8.0}_{-7.5}$	113^{+9}_{-9}	$26.4^{+4.2}_{-4.0}$	$1.12^{+0.08}_{-0.08}$
100906A	110.0-115.4	$0.02^{+0.01}_{-0.01}$	$89.3^{+10.3}_{-10.0}$	113^{+9}_{-9}	$31.5^{+4.7}_{-4.6}$	$1.10^{+0.08}_{-0.08}$
140512A	108.9-114.2	$0.37^{+0.02}_{-0.02}$	$1.7^{+0.1}_{-0.1}$	$95.5^{+1.2}_{-1.2}$	$1.0^{+0.0}_{-0.0}$	$0.99^{+0.09}_{-0.09}$
140512A	128.2-142.6	$0.40^{+0.00}_{-0.00}$	$3.6^{+0.1}_{-0.1}$	$95.8^{+0.4}_{-0.4}$	$2.1^{+0.0}_{-0.0}$	$1.19^{+0.05}_{-0.05}$
140512A	142.6-145.6	$0.28^{+0.05}_{-0.05}$	$1.4^{+0.2}_{-0.2}$	$82.9^{+5.1}_{-5.0}$	$1.3^{+0.1}_{-0.1}$	$0.96^{+0.09}_{-0.09}$
140512A	145.6-156.0	$0.22^{+0.02}_{-0.02}$	$1.2^{+0.1}_{-0.1}$	$86.2^{+2.2}_{-2.0}$	$0.9^{+0.0}_{-0.0}$	$1.04^{+0.08}_{-0.08}$
151027A	97.1-105.7	$0.31^{+0.04}_{-0.04}$	$1.6^{+0.2}_{-0.2}$	$81.6^{+3.6}_{-3.7}$	$1.5^{+0.1}_{-0.1}$	$1.09^{+0.08}_{-0.08}$
151027A	105.7-109.1	$0.39^{+0.01}_{-0.01}$	$4.2^{+0.2}_{-0.2}$	$94.6^{+1.0}_{-1.0}$	$2.5^{+0.1}_{-0.1}$	$1.05^{+0.07}_{-0.07}$
151027A	109.1-112.1	$0.38^{+0.01}_{-0.01}$	$5.6^{+0.2}_{-0.2}$	$94.7^{+1.0}_{-1.0}$	$3.3^{+0.1}_{-0.1}$	$1.07^{+0.08}_{-0.07}$
151027A	112.1-115.2	$0.35^{+0.04}_{-0.04}$	$4.5^{+0.4}_{-0.4}$	$86.5^{+2.8}_{-2.9}$	$3.5^{+0.2}_{-0.2}$	$1.14^{+0.08}_{-0.07}$
151027A	115.2-120.0	$0.21^{+0.04}_{-0.04}$	$3.2^{+0.4}_{-0.5}$	$77.5^{+5.0}_{-6.1}$	$3.5^{+0.3}_{-0.3}$	$1.20^{+0.08}_{-0.08}$
161117A	72.5-90.2	$0.07^{+0.01}_{-0.01}$	$20.1^{+2.3}_{-2.1}$	153^{+10}_{-7}	$2.8^{+0.2}_{-0.2}$	$0.93^{+0.08}_{-0.08}$
161117A	90.2-92.7	$0.09^{+0.02}_{-0.02}$	$35.7^{+5.6}_{-5.4}$	162^{+13}_{-13}	$4.2^{+0.4}_{-0.5}$	$1.00^{+0.09}_{-0.09}$
161117A	92.7-100.2	$0.07^{+0.01}_{-0.01}$	$35.5^{+2.8}_{-2.5}$	137^{+4}_{-4}	$7.0^{+0.4}_{-0.4}$	$1.08^{+0.09}_{-0.08}$
161117A	100.2-104.1	$0.08^{+0.01}_{-0.01}$	$52.2^{+4.6}_{-4.0}$	134^{+6}_{-5}	$10.9^{+0.7}_{-0.9}$	$1.05^{+0.09}_{-0.09}$
161117A	131.0-138.5	$0.09^{+0.01}_{-0.01}$	$36.0^{+2.2}_{-2.2}$	$97.4^{+0.8}_{-0.8}$	$19.6^{+1.1}_{-1.1}$	$1.01^{+0.07}_{-0.07}$
161117A	138.5-144.2	$0.05^{+0.01}_{-0.01}$	$26.9^{+2.5}_{-2.4}$	$94.1^{+1.3}_{-1.2}$	$16.2^{+1.3}_{-1.3}$	$0.94^{+0.09}_{-0.09}$

Note. We also include values of r_d, which is not one of the fit parameters, but obtained from the relation $r_d = r_{ph}/\tau = L\sigma_T/4\pi\tau\Gamma^3c^3m_p$, as given in Section 2.1.
(This table is available in machine-readable form.)

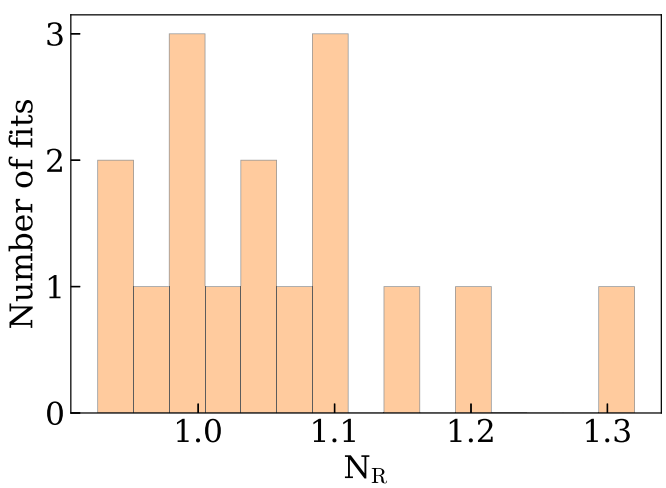

Figure 5. Histogram of the cross calibration constant. The histogram includes the 21 fits that passed the PPC.

all bursts, it may simply be a result of the small number of bins in the analysis.

We find no significant correlation between if a fit passes the PPC and the observed flux in the GBM or XRT, the S/N in any detector, or any of the model parameters obtained when fitting with a power law and cutoff-power law for the XRT and GBM data, respectively. Due to the small number of analyzed bins we cannot draw any strong conclusions from this.

6.3. Comparison to A19

The DREAM model was initially introduced in A15 where it was fit to two GRBs. In A19 we implemented significant improvements to the model and fit it to a larger sample of 36 GRBs. Here we have further tested the model by including XRT data at low energies in the analysis. This is because of the distinctive model predictions in this range, which result from the assumptions of internal shocks and negligible magnetization. The other main differences from A19 are that we have expanded the parameter space of the model slightly and analyzed the data using Bayesian inference. The model parameter space was extended with several new grid points in Γ, extending the grid down to $\Gamma = 50$ and up to $\Gamma = 1000$, and one point in $L_{0,52}$, extending it up to $L_{0,52} = 1000$. The joint GBM–XRT fits mainly inhabit the low-Γ part of this extended parameter space.

The higher $L_{0,52}$ and Γ would lead to additional accepted fits in the A19 sample. The difference in S/N cut would also lead to a larger number of analyzed spectra. Performing fits with the new model to the GBM data of the GRBs in the current sample primarily affects GRB 100728A and GRB 100906A. The fraction of accepted fits increases from 4% to 44% and from 26% to 41% in the bright interval before the XRT observations start for GRB 100728A and GRB 100906A, respectively. We note that these GRBs are still not fully described by the model and that the highest $L_{0,52}$ of both bursts push the limit of what is physically plausible.

One of the main conclusions of A19 was that DREAM is unable to account for the brightest GRBs. Figure 9 is

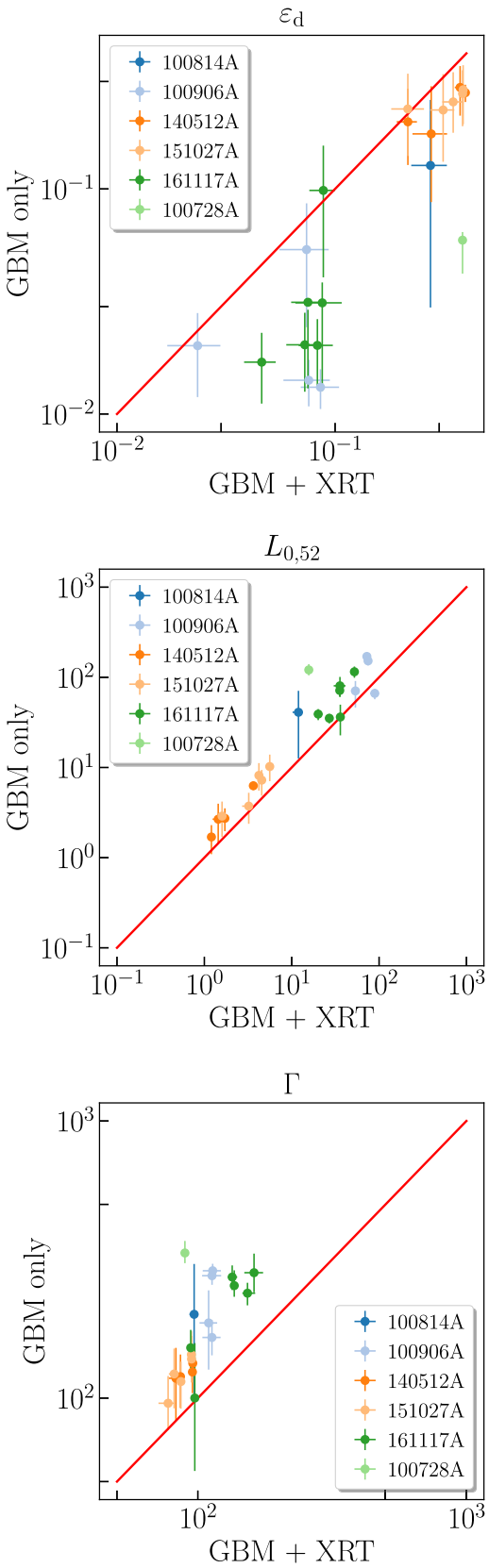

Figure 6. Comparison of parameter estimates from the analysis with and without XRT data. We show parameter estimates of the three free model parameters, ε_d, $L_{0,52}$, and Γ in the top, middle, and bottom panel, respectively. The red line corresponds to a 1: 1 relation. The figure only includes data points from fits that passed the PPC. The error bars represent the 1σ uncertainties.

reminiscent of the corresponding Figure 11 in A19, although the peak of the distribution is shifted to lower luminosities in this work (due to the sample in A19 being biased toward high-luminosity bursts). However, we do not observe the problem of under-predicting the observed luminosity in this analysis. Figure 9 can instead be attributed to the fact that higher luminosities result in less flexibility for the model. It is then harder to describe the data which results in high estimates of the luminosity, even when achieving a sufficiently high luminosity is not an issue. This was also discussed in A19. However, as pointed out in Section 6.2, Figure 9 could also be the result of the small number of analyzed spectra.

6.4. Implications of XRT Data

As noted in Section 5.2, the inferred parameter estimates change systematically as we add XRT data. However, for a majority of spectra, the changes are within reasonable uncertainties of the fits to the GBM-only data. Conversely, five spectra exhibit significant inconsistencies between the posterior of the joint GBM–XRT analysis and the GBM-only analysis, and are thus rejected, as discussed in Section 6.1. The fact that the XRT data make a significant difference in the analysis of prompt emission has also been found by Oganesyan et al. (2017, 2018). It is clear that there are spectra in this sample which the DREAM model cannot describe. This may of course be due to the fact that it simply does not represent the correct dissipation scenario or emission process for these bursts. However, there are also other possibilities that do not necessarily rule out the physical scenario considered here. We discuss these in turn below.

6.4.1. Presence of Additional Components

It is possible that the emission observed by XRT is of a (partly) different origin than that observed by GBM. Since DREAM is a one-zone model and we consider no additional components in the analysis, this could help explain some of the cases where we are unable to find good fits. Additional components can originate from different emission sites within the jet itself (e.g., an optically thin component), a region outside the jet (e.g., cocoon emission), or by interactions of the jet with the surrounding medium (e.g., afterglow). However, we note that all XRT light curves have flares, suggesting that this emission is closely related to prompt emission. Additionally, most light curves exhibit significant similarities in the GBM and XRT light curves (see Figure 1). The main difference that can be seen is that the XRT light curves are often stronger at the end of the bursts, resembling a kind of delay. This may reflect the commonly observed softening of the prompt emission, with the spectral peak moving to lower energies with time. A particularly clear example is GRB 151027A, which has very bright XRT emission peaking ∼15 s later than the GBM light curve. Additionally, GRB 100906A shows a similar delay while also having weak GBM emission in the overlap, leading to a clear difference in the light curve morphology between the XRT and GBM.

GRB 151027A is the only GRB in our sample with an extra component reported in the literature. Nappo et al. (2017) find a blackbody component at soft X-rays from joint fits to GBM, BAT, and XRT data. This was confirmed by Valan et al. (2018), performing an analysis of XRT data using a power law

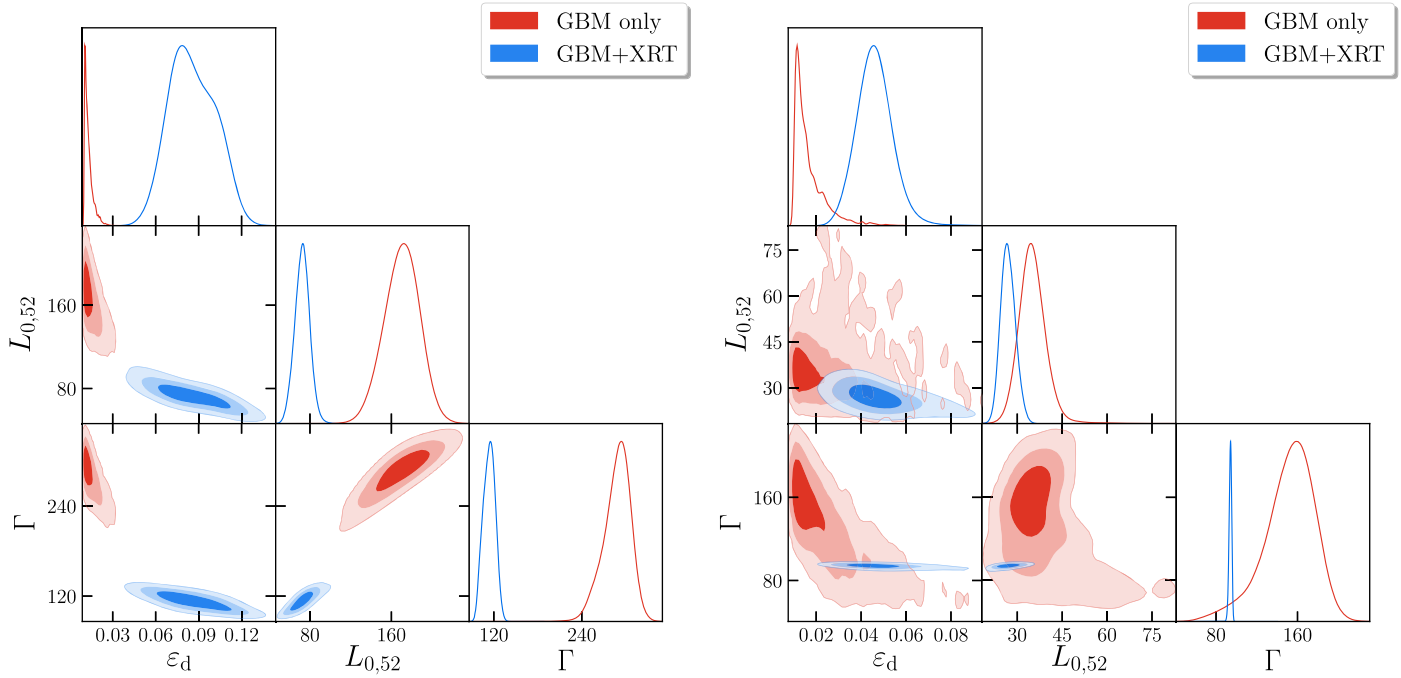

Figure 7. Posteriors for the joint GBM–XRT analysis and the analysis of GBM data only in blue and red, respectively. The left and right panels show the case of GRB 100906A at 100.5–105.0 s (the third time bin) and GRB 161117A at 138.5–144.2 s (the eighth time bin), respectively. The contours denote the 68%, 95% and 99.7% HPD regions. The fit in the left panel is rejected manually due to the disjunct posterior distributions, whereas the fit in the right panel shows an accepted fit. The complete figure set for all fits that passed the PPC (21 images) is available in the online journal.

(The complete figure set (21 images) is available.)

plus a blackbody. We note that the DREAM model provides adequate fits in the early times of XRT data, when the flux from the additional blackbody is low. When the blackbody becomes significant, we instead obtain a poor fit (see Nappo et al. 2017; Valan et al. 2018 for discussions on the blackbody flux). Nappo et al. (2017) suggest that the blackbody originates from the re-acceleration of the fireball. Another possibility is that the thermal component originates from a hot cocoon surrounding the jet, as discussed by Valan et al. (2018). Neither scenario can be described using the DREAM model, since it is a one-zone photospheric model with no hydrodynamical evolution. Alternatively, an extra blackbody component may indicate dissipation occurring just below the photosphere, which is known to produce double-peaked spectra (see A15). This scenario would not be captured by the current version of the model due to the assumption of dissipation at $\tau = 35$.

Performing the same analysis of the XRT data as in Valan et al. (2018), we find no significant blackbody in any of the other bursts. However, additional components may have different spectral shapes, which could account for the excess seen in some of the GRBs. This is unlikely to be the only explanation for all the poor fits though, as the model clearly fails to describe many intervals in GRBs where the light curves are well correlated (see Figure 1).

6.4.2. Model Implications

In A19 we argued that a different dissipation scenario than internal shocks is needed for the brightest GRBs. The study presented in this paper has revealed additional issues at soft X-rays in some bursts. Assuming no additional components are present, this suggests that the current implementation of the model does not capture all the relevant conditions and processes. Here we discuss what assumptions should be modified in order to better describe the observed data.

Because the parameter space was designed partially based on fits to GBM data, the introduction of XRT data provides new information on what the appropriate parameter space is. Examining the example in Figure 8, we note that the XRT data in the left plot are highly reminiscent of what we expect for synchrotron photons in the XRT energy range for our model. In Figure 11, we show examples of what model spectra look like using different values of the magnetization parameter, ε_b. Although the spectrum in Figure 8 can be successfully described by our model without synchrotron, the corresponding parameter estimates change. Using a model with synchrotron photons in the XRT energy range might provide an acceptable fit with smaller changes in parameter estimates. This is in no way proof of the presence of synchrotron photons, but it does provide us with strong motivation to expand the parameter space to test a scenario with a significant contribution from synchrotron radiation.

Additionally, the effects of geometric broadening are expected to be largest in the XRT energy range, (Lundman et al. 2013). The general effect of geometric broadening is a softening of the low-energy spectral slope, creating a relative excess of photons at these energies. This again resembles what we see in Figure 8, although the effect is expected to be smaller than what we see for ε_b. Expanding the parameter space in other free parameters, e.g., the optical depth, τ, could also help improve the fits. Tests conducted in A19 showed that this parameter has only a small impact on the fits. However, given the significantly tighter constraints provided by the XRT data, it is possible that τ would make a difference, since it governs the degree by which the seed blackbody is Comptonized. Particularly, a lower τ may help describe the double-peaked

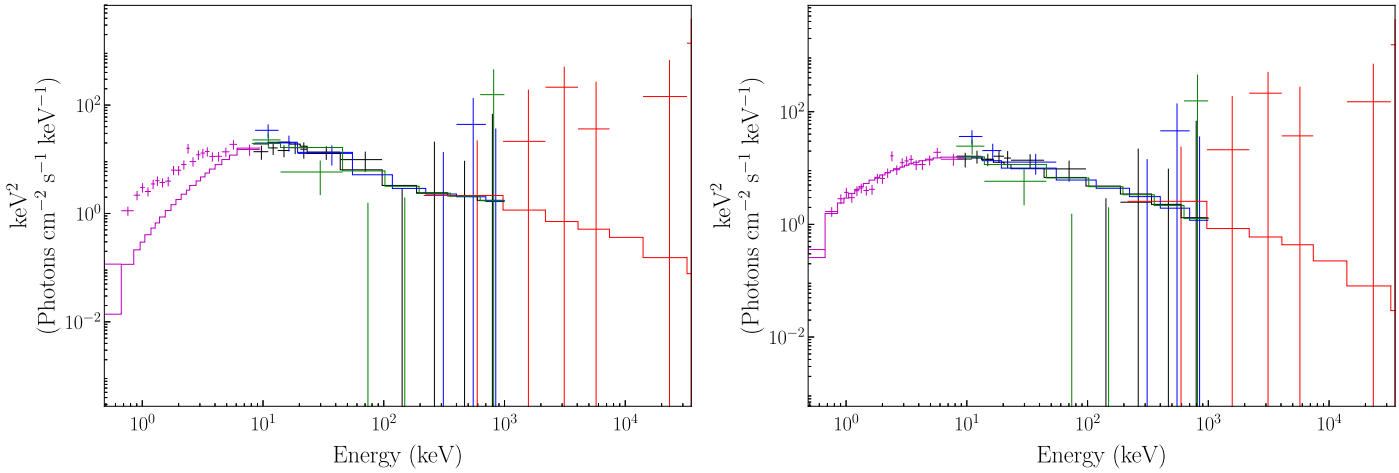

Figure 8. Examples of best-fit models to GRB 161117A at 138.5–144.2 s. The magenta, black, blue, green, and red colors represent data and model for the XRT, NaI2, NaI1, NaI10, and BGO0 detectors, respectively. The left panel shows the result of fitting DREAM1.3 to only the GBM data, with the XRT data being added to the figure without having been used in the analysis. Note that the extrapolation of the fit down to 0.3 keV includes absorption. The right panel shows the fit to all data. The parameters are $\varepsilon_d = 0.017$, $L_{0,52} = 35.2$, $\Gamma = 152$, and $\varepsilon_d = 0.046$, $L_{0,52} = 26.9$, $\Gamma = 94.1$ in the left and right plot, respectively. Our PPC accepts both the fit in the left (without the XRT data) and right figure. Note that plotting only the best-fit model in νF_ν is not the best representation of either the data or the posterior. This representation is chosen here to provide a qualitative comparison with model spectra for the discussion in Section 6.4.

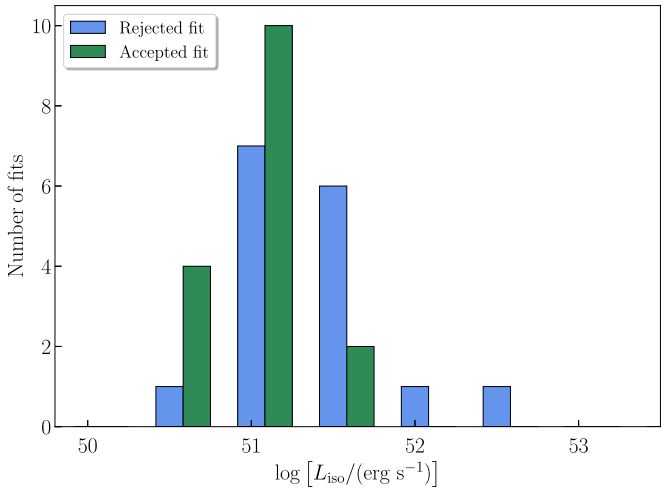

Figure 9. Histograms of the logarithm of the isotropic equivalent luminosity, L_{iso}. We show two bins per decade, spaced uniformly. The bars have been separated for visual clarity. Blue and green bars indicate fits which failed and passed the PPC, respectively. L_{iso} was obtained from fits with a cut-off power law.

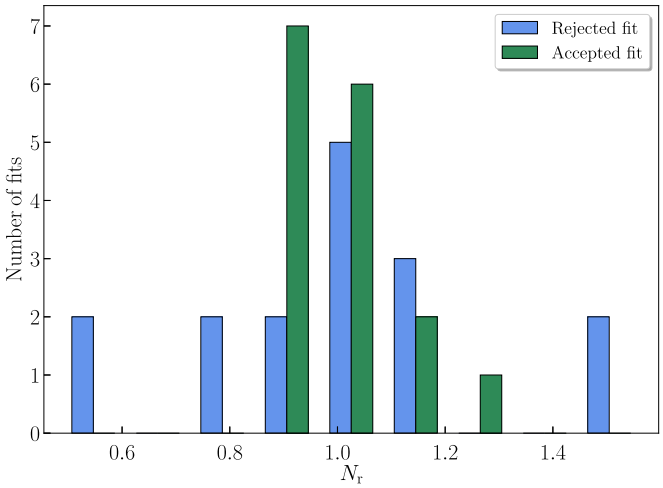

Figure 10. Histograms of the cross-calibration constant N_R. Blue and green bars indicate fits which failed and passed the PPC, respectively. The bars have been separated for visual clarity.

spectra in GRB 151027A, as discussed above. Thus, although the XRT data suggest that we should reject our current model for several bursts, there is additional parameter space which should be explored before rejecting the physical scenario altogether for these GRBs. The very large number of simulations required for this will be presented in a future work.

As noted above, almost all light curves exhibit some degree of lag between the GBM and XRT data. Apart from being caused by spectral evolution of the prompt emission or by separate emission processes, this discrepancy could originate from high-latitude emission (see e.g., Zhang et al. 2007). High-latitude emission has a lower Doppler boost than on-axis emission, which in the framework of our model would be identified as a lower Lorentz factor. Thus, the fact that we consistently find lower values of Γ when we include the XRT data is intriguing. If there is indeed significant high-latitude emission present in the overlapping time internal of XRT and GBM data, this could help explain the systematic shift to lower

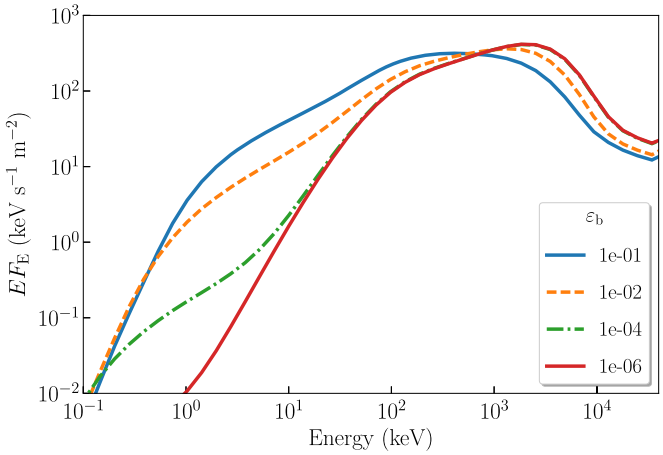

Figure 11. Example of how the model spectra change as a function of the energy dissipated into magnetic fields, ε_b. The model spectra in this figure were produced with $\varepsilon_d = 0.1$, $L_{0,52} = 50$, and $\Gamma = 300$. The values of ε_b for each spectrum are given by the legend.

Γ. If this is the case it indicates that we cannot neglect the geometry of the emission region at late times, when high-latitude emission becomes increasingly prevalent.

Finally, as discussed in A19, the assumption of internal shocks by setting $r_d = \Gamma^2 r_0$ should be re-evaluated. Letting r_0 be a free model parameter would allow us to set the blackbody temperature more freely. Since internal shocks are expected to have an efficiency on the order of 1%–10% (Mochkovitch et al. 1995; Kobayashi et al. 1997; Panaitescu et al. 1999) the increased values of ε_d when introducing the XRT data are also problematic. The internal shock assumption is also identified in A19 as a likely cause for the luminosity problem observed there. Thus, in order to further assess the scenario of subphotoshperic dissipation in GRBs, we must drop the assumption that $r_d = \Gamma^2 r_0$.

7. Summary and Conclusions

We have performed a time-resolved Bayesian analysis of all GRBs that have known redshifts and a significant overlap of GBM and XRT data. This gives us an energy range of 0.3 keV–40 MeV, which encapsulates most distinct spectral features predicted by many physical models. Following the work in A19, we have constructed and tested DREAM1.3, a table model for localized subphotospheric dissipation by internal shocks in a low-magnetization outflow. Our sample consists of eight GRBs which all have at least one spectrum with significant signal in both the XRT and GBM ($S/N > 3$). Binning the data with Bayesian blocks and performing the S/N cut, we obtain 32 spectra. We use a PPC complemented by a manual inspection to assess the quality of the fits. Our main results can be summarized as follows.

1. Sixteen of 32 analyzed spectra are well described by the model. No GRB is fully described by the model, but in three GRBs at least half of the fits are accepted.
2. The main problem for the model is a small excess of photons at low energies, relative to the extrapolation of the GBM-only fits. Even in the case of accepted fits, this leads to systematic changes in parameter estimates when we add the XRT data. Specifically, Γ and $L_{0,52}$ decrease whereas ε_d increases, albeit within the 3σ uncertainties of the GBM-only fits.
3. For GRB 151027A the sole rejected bin can likely be explained by the presence of an additional emission component, as previously reported by Nappo et al. (2017) and Valan et al. (2018).
4. The inclusion of XRT data have a large impact on model assessment and leads to much tighter parameter constraints than when using GBM-only data.

From these results we see that subphotospheric dissipation with internal shocks cannot describe all prompt emission. However, even for the GRBs where all analyzed spectra are rejected we cannot completely rule out this dissipation scenario. The model only has three free parameters and is thus a limited implementation of the physical scenario. It is encouraging that this simple implementation can describe half of the analyzed spectra. The following are the most promising future improvements.

1. The introduction of synchrotron photons. This is realized by letting ε_b be a free parameter.
2. Dissipation at different optical depths, characterized by the model parameter τ. In particular, low values of τ can result in double-peaked spectra (see A15). This is especially relevant for the case of GRB 151027A, where dissipation just below the photosphere is a possible alternative explanation for the rejected spectrum.
3. The removal of the assumption of internal shocks ($r_d = \Gamma^2 r_0$), such that r_0 is instead set independently of other model parameters. This would decouple the initial blackbody temperature, which sets the position of the low-energy cutoff, from Γ and $L_{0,52}$.

Implementation of these improvements will be presented in future work.

This work was supported by the Göran Gustafsson Stiftelse, the Swedish National Space Board and the Knut & Alice Wallenberg Foundation. The simulations were performed on resources provided by the Swedish National Infrastructure for Computing (SNIC) at the National Supercomputer Centre (NSC). F.R. is supported by the Göran Gustafsson Foundation for Research in Natural Sciences and Medicine. This work made use of data supplied by the UK Swift Science Data Centre at the University of Leicester.

Facilities: *Fermi*(GBM), *Swift*(XRT).

Software: astropy (Astropy Collaboration et al. 2013), PyMultiNest (Buchner et al. 2014), Xspec (Arnaud et al. 1999), SciPy (Jones et al. 2001), Matplotlib (Hunter 2007), Pandas (McKinney 2010), Seaborn (Waskom et al. 2014).

ORCID iDs

Björn Ahlgren https://orcid.org/0000-0003-4000-8341
Josefin Larsson https://orcid.org/0000-0003-0065-2933
Felix Ryde https://orcid.org/0000-0002-9769-8016
Asaf Pe'er https://orcid.org/0000-0001-8667-0889

References

Abdo, A. A., Ackermann, M., Arimoto, M., et al. 2009, Sci, 323, 1688
Ahlgren, B., Larsson, J., Ahlberg, E., et al. 2019, MNRAS, 485, 474
Ahlgren, B., Larsson, J., Nymark, T., Ryde, F., & Pe'er, A. 2015, MNRAS, 454, L31
Amati, L., Frontera, F., Tavani, M., et al. 2002, A&A, 390, 81
Arnaud, K., Dorman, B., & Gordon, C. 1999, XSPEC: An X-ray spectral fitting package, Astrophysics Source Code Library, ascl:9910.005
Arnaud, K. A. 1996, in ASP Conf. Ser. 101, Astronomical Data Analysis Software and Systems V, ed. G. H. Jacoby & J. Barnes (San Francisco, CA: ASP), 17
Band, D., Matteson, J., Ford, L., et al. 1993, ApJ, 413, 281
Bégué, D., Siutsou, I. A., & Vereshchagin, G. V. 2013, ApJ, 767, 139
Beloborodov, A. M. 2010, MNRAS, 407, 1033
Beloborodov, A. M. 2011, ApJ, 737, 68
Bhat, P. N., Meegan, C. A., von Kienlin, A., et al. 2016, ApJS, 223, 28
Bissaldi, E., von Kienlin, A., Lichti, G., et al. 2009, ExA, 24, 47
Briggs, M. S., Band, D. L., Kippen, R. M., et al. 1999, ApJ, 524, 82
Buchner, J., Georgakakis, A., Nandra, K., et al. 2014, A&A, 564, A125
Burgess, J. M. 2017, in Proc. 7th Int. Fermi Symp. 74 (Trieste: SISSA)
Burgess, J. M., Bégué, D., Bacelj, A., et al. 2018, arXiv:1810.06965
Burgess, J. M., Bégué, D., Ryde, F., et al. 2016, ApJ, 822, 63
Burgess, J. M., Preece, R. D., Connaughton, V., et al. 2014, ApJ, 784, 17
Burgess, J. M., Yu, H.-F., Greiner, J., & Mortlock, D. 2018, MNRAS, 476, 1427
Burrows, D. N., Falcone, A., Chincarini, G., et al. 2007, RSPTA, 365, 1213
Burrows, D. N., Hill, J. E., Nousek, J. A., et al. 2005, SSRv, 120, 165
Campana, S., Salvaterra, R., Melandri, A., et al. 2012, MNRAS, 421, 1697
Cash, W. 1979, ApJ, 228, 939
Chhotray, A., & Lazzati, D. 2015, ApJ, 802, 132
Chincarini, G., Mao, J., Margutti, R., et al. 2010, MNRAS, 406, 2113

Daigne, F., & Mochkovitch, R. 1998, MNRAS, 296, 275
Feroz, F., & Hobson, M. P. 2008, MNRAS, 384, 449
Feroz, F., Hobson, M. P., & Bridges, M. 2009, MNRAS, 398, 1601
Feroz, F., Hobson, M. P., Cameron, E., & Pettitt, A. N. 2013, arXiv:1306.2144
Gelman, A., li Meng, X., & Stern, H. 1996, Statistica Sinica, 6, 733
Gelman, A., & Shalizi, C. R. 2013, British Journal of Mathematical and Statistical Psychology, 66, 8
Ghirlanda, G., Nappo, F., Ghisellini, G., et al. 2018, A&A, 609, A112
Ghirlanda, G., Pescalli, A., & Ghisellini, G. 2013, MNRAS, 432, 3237
Giannios, D. 2006, A&A, 457, 763
Goldstein, A., Burgess, J. M., Preece, R. D., et al. 2012, ApJS, 199, 19
Golenetskii, S. V., Mazets, E. P., Aptekar, R. L., & Ilinskii, V. N. 1983, Natur, 306, 451
Hunter, J. D. 2007, CSE, 9, 90
Ito, H., Matsumoto, J., Nagataki, S., et al. 2019, NatCo, 10, 1504
Jones, E., Oliphant, T., Peterson, P., et al. 2001, SciPy: Open source scientific tools for Python, http://www.scipy.org/
Kobayashi, S., Piran, T., & Sari, R. 1997, ApJ, 490, 92
Larsson, J., Racusin, J. L., & Burgess, J. M. 2015, ApJL, 800, L34
Lazzati, D., Morsony, B. J., & Begelman, M. C. 2009, ApJL, 700, L47
Lloyd, N. M., & Petrosian, V. 2002, ApJ, 565, 182
Lü, J., Zou, Y.-C., Lei, W.-H., et al. 2012, ApJ, 751, 49
Lundman, C., Pe'er, A., & Ryde, F. 2013, MNRAS, 428, 2430
Lynch, S. M., & Western, B. 2004, Sociological Methods & Research, 32, 301
McKinney, W. 2010, in Proc. 9th Python in Science Conf., ed. S. van der Walt & J. Millman (Austin, TX: SciPy), 51, http://conference.scipy.org/proceedings/scipy2010/mckinney.html
Meegan, C., Lichti, G., Bhat, P. N., et al. 2009, ApJ, 702, 791
Meng, X.-L. 1994, AnSta, 22, 1142
Mochkovitch, R., Maitia, V., & Marques, R. 1995, Ap&SS, 231, 441
Nappo, F., Pescalli, A., Oganesyan, G., et al. 2017, A&A, 598, A23
O'Brien, P. T., Willingale, R., Osborne, J., et al. 2006, ApJ, 647, 1213
Oganesyan, G., Nava, L., Ghirlanda, G., & Celotti, A. 2017, ApJ, 846, 137
Oganesyan, G., Nava, L., Ghirlanda, G., & Celotti, A. 2018, A&A, 616, A138
Panaitescu, A., Spada, M., & Mészáros, P. 1999, ApJL, 522, L105
Parsotan, T., López-Cámara, D., & Lazzati, D. 2018, ApJ, 869, 103
Pe'er, A. 2008, ApJ, 682, 463
Pe'er, A. 2015, AdAst, 2015, 907321
Pe'er, A., Mészáros, P., & Rees, M. J. 2006, ApJ, 642, 995
Pe'er, A., & Waxman, E. 2005, ApJ, 628, 857
Planck Collaboration, Ade, P. A. R., Aghanim, N., et al. 2014, A&A, 571, A16
Preece, R. D., Briggs, M. S., Mallozzi, R. S., et al. 1998, ApJL, 506, L23
Racusin, J. L., Liang, E. W., Burrows, D. N., et al. 2009, ApJ, 698, 43
Rees, M. J., & Mészáros, P. 2005, ApJ, 628, 847
Astropy Collaboration, Robitaille, T. P., Tollerud, E. J., et al. 2013, A&A, 558, A33
Rubin, D. B. 1984, AnSta, 12, 1151
Ryde, F. 2004, ApJ, 614, 827
Ryde, F., Pe'er, A., Nymark, T., et al. 2011, MNRAS, 415, 3693
Scargle, J. D., Norris, J. P., Jackson, B., & Chiang, J. 2013, arXiv:1304.2818
Tavani, M. 1996, ApJ, 466, 768
Valan, V., Larsson, J., & Ahlgren, B. 2018, MNRAS, 474, 2401
Verner, D. A., Ferland, G. J., Korista, K. T., & Yakovlev, D. G. 1996, ApJ, 465, 487
Vianello, G. 2018, ApJS, 236, 17
Vurm, I., Beloborodov, A. M., & Poutanen, J. 2011, ApJ, 738, 77
Waskom, M., Botvinnik, O., Hobson, P., et al. 2014, seaborn: v0.5.0, Zenodo, doi:10.5281/zenodo.12710
Willingale, R., Starling, R. L. C., Beardmore, A. P., Tanvir, N. R., & O'Brien, P. T. 2013, MNRAS, 431, 394
Wilms, J., Allen, A., & McCray, R. 2000, ApJ, 542, 914
Yonetoku, D., Murakami, T., Nakamura, T., et al. 2004, ApJ, 609, 935
Yonetoku, D., Murakami, T., Tsutsui, R., et al. 2010, PASJ, 62, 1495
Zhang, B., & Yan, H. 2011, ApJ, 726, 90
Zhang, B.-B., Liang, E.-W., & Zhang, B. 2007, ApJ, 666, 1002
Zhang, B.-B., Uhm, Z. L., Connaughton, V., Briggs, M. S., & Zhang, B. 2016, ApJ, 816, 72